

See discussions, stats, and author profiles for this publication at: <https://www.researchgate.net/publication/270576430>

Intercalation and Confinement of Poly(ethylene oxide) in Porous Carbon Nanoparticles with Controlled Morphologies

ARTICLE in *MACROMOLECULES* · DECEMBER 2014

Impact Factor: 5.8 · DOI: 10.1021/ma501607e

CITATIONS

3

READS

42

7 AUTHORS, INCLUDING:



[Fabienne Barroso-Bujans](#)

Center of Materials Physics

45 PUBLICATIONS 734 CITATIONS

SEE PROFILE



[Pablo Palomino](#)

Complutense University of Madrid

16 PUBLICATIONS 22 CITATIONS

SEE PROFILE



[Felix Fernandez-Alonso](#)

Science and Technology Facilities Council

136 PUBLICATIONS 1,155 CITATIONS

SEE PROFILE



[Juan Colmenero](#)

Universidad del País Vasco / Euskal Herriko U...

402 PUBLICATIONS 8,552 CITATIONS

SEE PROFILE

Intercalation and Confinement of Poly(ethylene oxide) in Porous Carbon Nanoparticles with Controlled Morphologies

Fabienne Barroso-Bujans,^{*,†,‡} Pablo Palomino,[§] Felix Fernandez-Alonso,^{||,⊥} Svemir Rudić,^{||} Angel Alegría,^{†,#} Juan Colmenero,^{†,‡,#} and Eduardo Enciso[§]

[†]Centro de Física de Materiales (CSIC-UPV/EHU)-Materials Physics Center, Paseo Manuel Lardizábal 5, 20018 San Sebastián, Spain

[‡]Donostia International Physics Center, Paseo Manuel Lardizábal 4, 20018 San Sebastián, Spain

[§]Departamento de Química Física I, Facultad de Ciencias Químicas, Universidad Complutense, 28040 Madrid, Spain

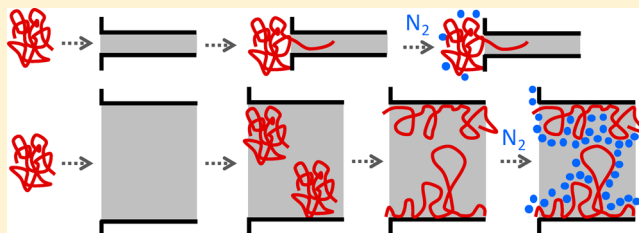
^{||}ISIS Facility, Rutherford Appleton Laboratory, Chilton, Didcot, Oxfordshire OX11 0QX, United Kingdom

[⊥]Department of Physics and Astronomy, University College London, Gower Street, London WC1E 6BT, United Kingdom

[#]Departamento de Física de Materiales, Universidad del País Vasco (UPV/EHU) Apartado 1072, 20080 San Sebastián, Spain

Supporting Information

ABSTRACT: Polymers confined at the nanometer scale often exhibit a distinct structural and dynamical response compared to their bulk counterparts. In this study, we observe that the confinement of poly(ethylene oxide) (PEO) in the nanopores of carbon nanoparticles (CNPs) leads to the suppression of crystallization and to a significant reduction of the ΔC_p at the glass transition. We ask whether these changes are dominated by interfacial interactions (van der Waals type) or by geometrical constraints. For pore diameters below 2 nm (micropores following IUPAC nomenclature), we find that the larger the pore surface, the higher the amount of PEO intercalated in the micropores and, consequently, the larger the reduction of the ΔC_p at the glass transition (up to 50%). For pore diameters in the range 2–50 nm (mesopores), larger pore surfaces lead to a higher amount of PEO adsorbed on the mesopore walls and the smaller the reduction of the ΔC_p at the glass transition. Under these conditions of spatial confinement at the nanoscale, PEO chains cannot arrange themselves into large crystalline domains, as evidenced by a negligible degree of crystallization of at most 1.8%. High-resolution inelastic neutron scattering data show that the PEO chains confined in the pores of CNP adopt a planar zigzag conformation, which is distinctly different from those characteristic of the 7/2 helical structure of the bulk crystal.



INTRODUCTION

Understanding and predicting the structure and dynamics of polymers confined at nanometer length scales remain major challenges in polymer science.¹ A crucial aspect of experimental studies is that polymer–substrate interactions are always present, making it difficult to provide a consistent interpretation of the results. On the one hand, when the confining length scale (interlayer space in layered materials,^{2–4} pore diameter in porous substrates,⁵ or layer thickness in thin films⁶) is comparable to or smaller than the radius of gyration (R_g) of the free polymer, the influence of polymer–surface interactions on the structure and dynamics of the trapped chains cannot be neglected. On the other hand, when the confining length scale is larger than the R_g of the free polymer, different scenarios of confinement may be at play at the same time: (a) confinement due to surface adsorption whereby a thin adsorbed polymer layer is formed and (b) geometrical confinement of the inner polymer chains. In the latter, surface interactions tend to be screened by the surface-adsorbed polymer layer. Numerous studies have observed systematic changes in the dynamics of confined polymers via modification of the nature of polymer/

substrate interactions. Some examples include the study of the segmental and normal modes of polymers confined in hydrophilic and hydrophobic porous glasses,⁵ the formation of self-assembled polymers with frustrated phases when confined in reduced geometries with variable surface affinity,⁷ and studies of the glass-transition temperature of thin films supported on different substrates.^{8–10} In terms of practical applications, carbon-based nanostructured materials have been extensively investigated due to their light weight, low cost, and high surface area for the design of conducting-polymer nanocomposites^{11,12} as well as three-dimensional macroporous materials^{13–15} based on carbon nanotubes, carbon nanofibers, and graphene with applications as electrodes in fuel cells, Li-ion batteries, and supercapacitors. In these applications, the physicochemical properties of the adsorbed polymer layer are of paramount importance. If, for example, the glass transition and crystallization behavior of the polymer layer change due to

Received: August 4, 2014

Revised: October 28, 2014

Published: December 3, 2014

confinement, our understanding of these effects becomes central for a detailed assessment of their potential use in practical applications.

In the above context, we have recently shown that the crystallization and underlying segmental mobility of poly(ethylene oxide) (PEO) are largely affected by confinement in the nanometer-scale pores of organic resins and carbon nanoparticles.¹⁶ The high surface affinity of the polymer to the resin, induced by hydrogen-bond interactions, led to a strong (almost complete) suppression of the calorimetric glass-transition temperature (T_g) of the confined PEO phase. This effect was less pronounced in PEO confined in the pores of carbon nanoparticles, although we estimated a loss of 30% of cooperative dynamics at T_g . In this case, PEO–substrate interactions are mostly of the van der Waals type, typically weaker than hydrogen bonds. Another parameter that remains largely unexplored relates to the influence of the pore structure of the carbon nanoparticles on the physicochemical properties of PEO retained in the pores.

In this work, we study the effects of pore size of carbon nanoparticles (CNPs) on the glass transition and crystallization of confined PEO. In this situation, polymer/substrate interactions are predominantly of the van der Waals type. The pore structures of pristine and polymer-filled CNPs have been characterized in detail by nitrogen physisorption, providing access to both qualitative and quantitative information on the porosity of the substrates before and after PEO treatment. Polymer uptake as well as the structure and thermodynamics of PEO confined in CNP pores are discussed on the basis of the distinct topology of the substrate, including its volume, pore surface, and diameter. To this end, we have characterized the polymer phase by temperature-modulated differential scanning calorimetry (TM-DSC) and high-resolution inelastic neutron scattering (INS).

■ EXPERIMENTAL SECTION

Materials. The following compounds were used in the present work: resorcinol [$(C_6H_4(OH)_2)$, Sigma-Aldrich, 99%], formaldehyde aqueous solution [(H_2CO) , Panreac, 37–38%], sodium hydroxide [$(NaOH)$, Sigma-Aldrich, >97%], deionized water (obtained from a Direct Q5 Millipore system), and poly(ethylene oxide) [(PEO), Aldrich, $M_n = 9.4 \times 10^4$ g/mol and polydispersity index 1.08].

Methods. Organic resins were synthesized by polycondensation of resorcinol (R) and formaldehyde (F) in aqueous solution following the approach of Pekala et al.¹⁷ To obtain nanoparticles with different pore structure, the reactions were performed at different pH by adding appropriate amounts of sodium hydroxide and keeping the R-to-F molar ratio (R/F) at 0.5. In this process, sodium hydroxide (hereafter referred to as C) also acts as catalyst. The resulting solutions were then placed in an oven at 85 °C for 3 days. The color of the solutions changed progressively from clear to orange, then to red, and finally to dark brown over the course of the reaction. After the curing process, the gels were dried at 85 °C at ambient pressure over the course of two additional days, leading to the formation of dry organic resins. Finally, CNPs were obtained by pyrolysis of the organic resins at 900 °C for 4 h in a nitrogen atmosphere using a heating rate of 3 °C/min and a cooling rate of 5 °C/min. Table 1 summarizes the organic resins synthesized by varying R-to-C ratios (R/C) and pH.

PEO-filled CNP samples (PEO/CNPs) were prepared from aqueous solutions consisting of 1 g of PEO and 1 g of CNPs codissolved in 40 mL of water. The mixture was stirred for 15 days to enable the filling of the CNP galleries via the diffusion of the polymer chains into the cavities. Excess PEO was removed by centrifugation and repeated aqueous washings. The resulting PEO/CNP samples were dried at 80 °C in vacuo for 24 h and stored at room temperature under vacuum.

Table 1. Summary of CNP Synthesis Conditions from Organic Resins^a

organic resins/CNPs	pH	R/C ^b (mol/mol)
A	7.2	100
B	7.1	125
C	6.7	230
D	6.7	250
E	6.5	330
F	6.4	400
G	6.3	500
H	6.2	600
I	6.1	750

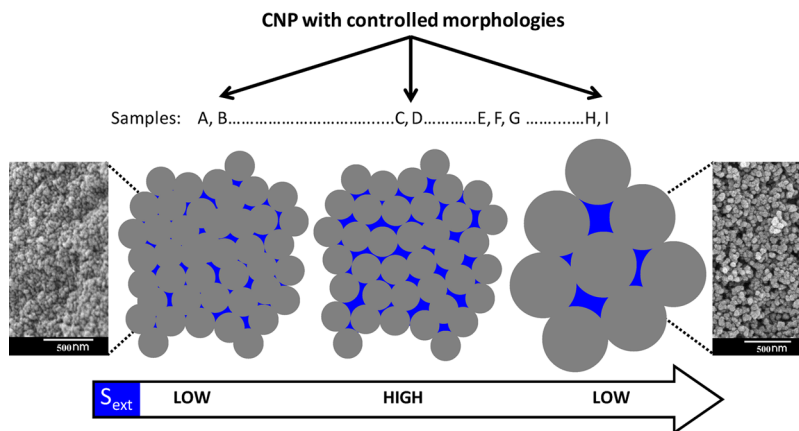
^aFor further details see the text. ^bR/C: resorcinol-to-catalyst (NaOH) ratio.

Characterization. The chemical composition of the CNPs was obtained from elemental analysis. The morphology and pore structure of pristine and PEO-filled CNPs were analyzed by field-emission scanning electron microscopy (FESEM) and nitrogen adsorption–desorption isotherms,¹⁸ respectively. FESEM images were collected with a JEOL JSM-6700F instrument operating at 5–10 kV and 12 μ A. The powder samples were supported on adhesive carbon tape and coated with a thin gold film. Nitrogen isotherms were obtained at 77 K using a Micromeritics ASAP 2020. CNPs were outgassed at 180 °C for 1 h, and PEO-containing samples were outgassed at 110 °C for 6 h. The specific surface area (S_{BET}) was determined from the linear part of the BET plot ($P/P_0 = 0.05–0.2$).¹⁹ External surface areas (S_{ext}) and micropore volumes (V_{mic}) were determined from the t -plots obtained via recourse to the Harkins–Jura equation.²⁰ Average pore diameters ($\langle d \rangle_{BJH}$) and mesopore volumes (V_{BJH}) were calculated with the Barrett–Joyner–Halenda (BJH) adsorption–desorption method²¹ assuming cylindrical pores in the Kelvin equation.²² Pore size distributions (PSDs) were obtained by applying the density functional theory (DFT) method to the nitrogen adsorption isotherms.¹⁸

PEO mass uptake in CNPs was determined by thermogravimetry (TGA) using a Q500 thermogravimetric analyzer from TA Instruments. Samples were heated from room temperature to 800 °C at a rate of 10 °C/min under a constant N_2 flow of 60 mL/min. The amount of PEO in PEO/CNPs was calculated from sample-residue analysis at 650 °C. These data show that intercalated PEO in CNP pores decomposes at 358 °C (see Figure S1 in the Supporting Information). On the basis of this protocol, the amount of PEO in PEO/CNP is given by $W_{PEO/CNP} = f_{CNP}W_{CNP} + f_{PEO}W_{PEO}$, where $W_{PEO/CNP}$, W_{CNP} , and W_{PEO} are the weight percentages of PEO/CNP, CNP, and PEO residues at 650 °C, respectively, and f_{CNP} and f_{PEO} are the mass fractions of CNP and PEO in PEO/CNP, respectively. Since $f_{PEO} = 1 - f_{CNP}$, mass balance allows us to write $f_{PEO} = (W_{CNP} - W_{PEO/CNP})/(W_{CNP} - W_{PEO})$.

Temperature-modulated differential scanning calorimetry (TM-DSC) measurements were carried out using a TA Instruments Q2000 on ~12 mg specimens sealed in aluminum pans. PEO/CNP samples and bulk PEO were first heated to 100 °C at the highest attainable heating rate and holding the temperature for 10 min at 100 °C. Then, samples were cooled to –150 °C in TM mode with a 0.48 °C temperature amplitude, 60 s modulation period, and 3 °C/min underlying cooling rate. Next, all samples were heated back to 100 °C at 5 °C/min. A helium flow rate of 25 mL/min was used all throughout. The TM-DSC data presented below are presented in terms of the reversing heat capacity (rev C_p) and nonreversing heat flow (or non-rev HF, that is the total heat flow minus the reversing heat flow). The nonreversing calorimetric signals primarily contain information on time-dependent thermal phenomena, whereas the reversing signals are dominated by the inherent thermal properties of the material such as heat capacity (C_p).²³

High-resolution INS data were collected on the TOSCA spectrometer²⁴ located at the ISIS Facility, Rutherford Appleton Laboratory, UK. TOSCA is a so-called indirect geometry time-of-flight

Scheme 1. Mesopore Areas (Blue) in Different CNP Specimens^a

^aSamples A and B are formed by a high coalescence of small diameter CNPs (15–20 nm diameter), creating small mesopore volumes between particles. As a result, S_{ext} in samples A and B is low. CNP coalescence in samples C and D is lower than in samples A and B for similar nanoparticle diameters. As a result, S_{ext} increases in samples C and D. Samples H and I are formed by larger diameter CNPs (up to 80 nm diameter), creating a high mesopore volume between particles. As a result, S_{ext} decreases.

neutron spectrometer spanning an energy-transfer range up to 4000 cm^{-1} in neutron energy loss with a spectral resolution of $\sim 1.5\%$. INS time-of-flight spectra were collected in both back- and forward-scattering geometries and then added together to obtain hydrogen-projected vibrational densities of states (VDOS). Typical run times varied between 2 and 8 h depending on the hydrogen content of the sample. All samples were contained in flat aluminum cells of thickness 1–4 mm and cooled to temperatures below 30 K. INS data of the empty aluminum cell were first subtracted from the data of all samples. Then, mass-normalized INS data of a given CNP were subtracted from the data of the corresponding PEO/CNP specimen. Finally, the resulting data were normalized to the amount of PEO content in the sample, as determined by TGA. INS data of bulk PEO were normalized to sample mass.

RESULTS AND DISCUSSION

Pore-Structure Characterization of CNPs. CNPs with variable surface area, pore volume, and pore diameter were synthesized via a thorough control of reaction time, concentration, and temperature program as described in the Experimental Section. CNPs are predominantly composed of spherical nanoparticles of ca. 15–80 nm diameter, which themselves are agglomerates of smaller particles. Interstitials between nanoparticles constitute mesopores ($2 < d < 50$ nm, where d is the pore diameter). Voids between the smaller particles form micropores ($d < 2$ nm).¹⁸ Additionally, high micropore areas are formed in CNPs during the pyrolysis of resin–nanoparticle precursors at 900 °C, a process whereby volatile compounds are released generating nanochannels throughout the carbon material.¹⁶ Nitrogen isotherms for all CNP samples conform to type IV with a type H1 hysteresis loop.²⁵ This loop is typically associated with capillary condensation in the mesopores.²⁵ Compositional data of the CNP materials indicate that nanoparticles are mainly composed of carbon (93 wt %), with only 6 wt % of oxygen and 1 wt % of hydrogen.

Scheme 1 illustrates the CNPs reported in Table 1. These CNPs are characterized by different morphologies, from highly coalesced, small diameter nanoparticles to slightly coalesced, larger diameter nanoparticles. Samples A and B are essentially composed of highly coalesced nanoparticles with poorly interconnected mesopores. Samples C and D contain moderately coalesced particles of similar dimensions to A and

B, thereby allowing a high interconnectivity across mesopores. Figure 1 shows CNP pore-structure parameters as obtained

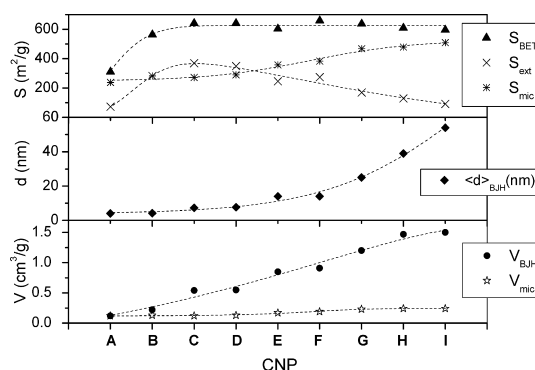


Figure 1. Pore-structure parameters of CNP specimens. For further details, see the text.

from nitrogen physisorption experiments. The external surface area (S_{ext}) characterizing the mesopores exhibits a maximum at 370 m^2/g (sample C) as a result of moderate coalescence and relatively small nanoparticle diameters. By increasing the nanoparticle diameter from sample C to I, we observe a monotonic increase of mesopore average diameter ($\langle d \rangle_{\text{BJH}}$) from 7 to 54 nm, a concomitant decrease of S_{ext} , and an increase of micropore areas (S_{mic}). The BET surface area ($S_{\text{BET}} \approx S_{\text{mic}} + S_{\text{ext}}$) remains fairly constant along the C-to-I series. Mesopore (V_{BJH}) and micropore volumes (V_{mic}) increase monotonically across this CNP series, exhibiting a higher increase in V_{BJH} relative to V_{mic} . Nitrogen isotherms were measured twice, from which we infer a 7% instrumental error in the determination of the above-mentioned parameters.

Pore-Structure Characterization of PEO/CNPs. SEM images of representative CNP and PEO/CNP specimens (sample I) are shown in Figure 2. The images show a globular morphology with a ~ 80 nm diameter in both samples indicating that the primary component in PEO/CNP is the CNP. In PEO/CNPs, we find no clear evidence for the presence of bulk PEO in the sample. These observations indicate that the absorbed PEO phase has been predominantly

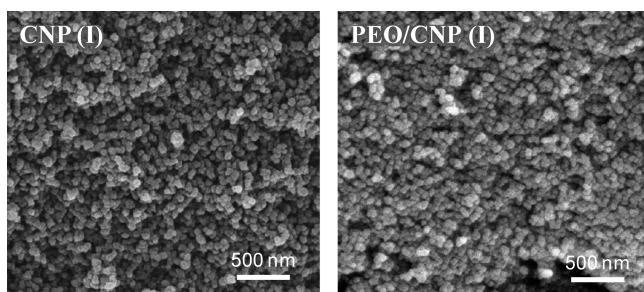


Figure 2. SEM images of a representative CNP and PEO/CNP (sample I).

intercalated within the CNP pores. The DSC and INS data presented below corroborate this picture and provide further and firm evidence for the existence of a distinct PEO phase in PEO/CNP markedly different from the bulk polymer.

PEO mass uptakes in the different CNP specimens are reported in Figure 3. The data show an increase in polymer

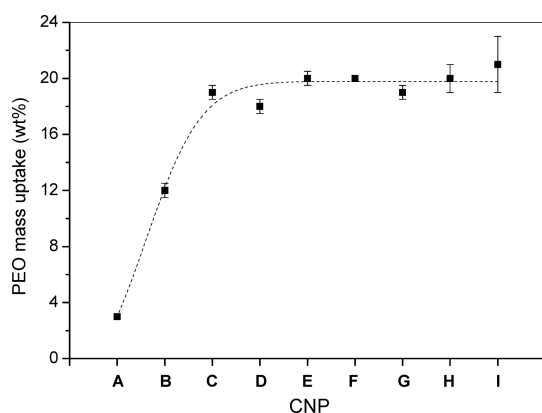


Figure 3. PEO mass uptake in different CNP specimens. Error bars were estimated from repeated TGA acquisitions of two independent samples.

absorption from a meagre 3% up to a saturation value of 20%. We note that the BET surface area (S_{BET}) of pristine CNP is the only pore-structure parameter showing a similar trend as polymer uptake across the CNP series studied in the present work (see Figure 1). However, a reduction of PEO mass uptake by 85% upon a 50% reduction of CNP S_{BET} (from sample C to A) indicates that other factors aside from surface area can also affect polymer uptake. One of these factors can be the poor mesopore interconnectivity described above for samples A and B. These samples display small average mesopore diameters ($\langle d \rangle_{\text{BJH}} < 4$ nm for A and $\langle d \rangle_{\text{BJH}} = 4$ for B), which are easily obstructed upon polymer absorption. Since the saturation value of PEO mass uptake in our samples is observed for CNPs with $\langle d \rangle_{\text{BJH}} > 7.5$ nm, it is likely that pores with $\langle d \rangle_{\text{BJH}} \leq 7$ nm form bottlenecks preventing further access of PEO to the pores.

Figure 4 shows the pore size distribution (PSD) for pristine and polymer-filled CNP samples. The shadowed areas shown below the difference curves represent the loss of pore volume upon PEO treatment. Neat CNP samples show a sharp peak at $d < 2$ nm (micropores) and a broad PSD at $d > 2$ nm (mesopores). Upon polymer treatment, the PSD curves show a notable decrease in nitrogen uptake. For instance, PEO/CNP (A) shows an almost complete suppression of nitrogen uptake, indicating that the polymer chains obstruct molecular

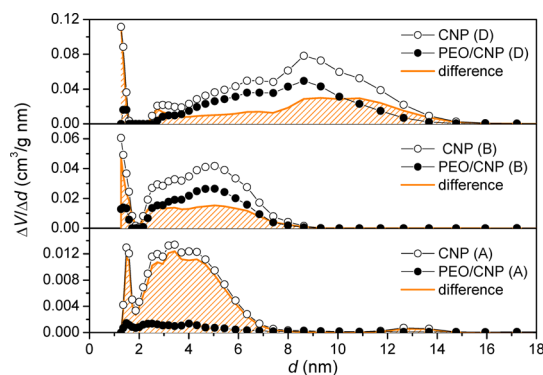


Figure 4. Pore size distribution (PSD) for representative samples of pristine and PEO-filled CNPs obtained by the DFT method. The shadowed areas correspond to the difference between the PSD data of PEO/CNP and CNP samples. $\Delta V/\Delta d$ (see ordinate axis) corresponds to the differential pore-volume distribution.

adsorption inside micro- and mesopores. This result demonstrates either an efficient occupancy of mesopores by PEO chains or a partial occupancy with subsequent blockage of the smaller pores. The low polymer uptake observed for this sample (only 3 wt %) suggests that the latter case is more likely than the former. Sample B represents a distinctly different situation. In this case, the PSD does not change appreciably upon polymer adsorption but the relative abundance of mesopores decreases by 40% compared to the pristine CNP. The shadowed area in Figure 4 shows a uniform occupancy of mesopores with different pore size. In sample D, the PSD of larger mesopores shows a stronger suppression of nitrogen uptake compared to the smaller pores. The shadowed area shows a higher occupancy of pores with $d > 8$ nm. This result suggests a preferential occupation of the larger mesopores by the confined polymer phase, where the PEO chains are likely to undergo adsorption on the mesopore walls, thereby reducing their effective diameter. In all cases, pores with $d < 2$ nm show an 80–90% reduction in nitrogen uptake, indicating the blockage to nitrogen access either because the polymer phase fills the pores or because the polymer chains block the pore entrance.

Other noteworthy features of PEO confinement in CNPs relate to mass-uptake saturation values, these being as high as ~ 20 wt % for samples C to I. The PEO adsorption isotherm as a function of PEO concentration in solution follows a Langmuir-type curve (Figure S2 in the Supporting Information), implying that the entrance of PEO into the pores depends on the interactions with the CNP surface. Furthermore, extrapolation of polymer uptake to a PEO concentration of 25 mg/mL (uptake experiments) yields 0.25 ± 0.02 g of PEO/g of CNP (20 wt % of the total mass). This value reproduces the saturation level found in our experiments, as shown in Figure 3. We can also estimate the area occupied by the PEO chains confined in CNPs by considering the density of bulk PEO (1.14 g cm^{-3}) and a thickness of a PEO monolayer of 3.4 \AA .⁴ Using these values, we obtain that 20 wt % of PEO in PEO/CNP samples corresponds to an area of 600–640 m^2/g , a figure which translates into a coverage of $\sim 100\%$ of the BET surface area.

Since the CNPs display a similar S_{BET} as a result of an increasing S_{mic} and a decreasing S_{ext} in going from sample C to I, it is likely that the fraction of polymer confined within the micropores increases with increasing S_{mic} and subsequently, the

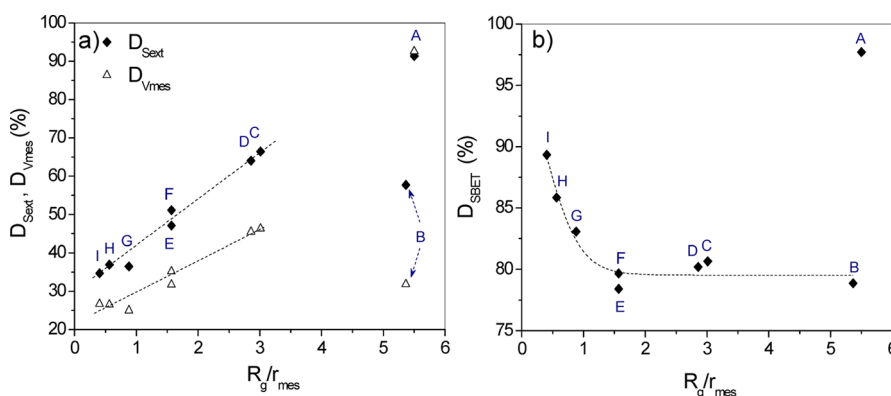


Figure 5. Relative decrease of (a) external surface/mesopore volume ($D_{S_{ext}}/D_{V_{mes}}$) and (b) BET area ($D_{S_{BET}}$) of CNPs upon PEO absorption as a function of the ratio of the radius of gyration of PEO to average mesopore radius.

fraction of polymer confined within the mesopores decreases with decreasing S_{ext} in such a way that the resulting amount of polymer confined in the sample remains constant. Therefore, the relative amount of PEO in both micropores and mesopores varies along the different samples. The higher the S_{mic} , the higher the fraction of polymer confined in the micropores. Likewise, the higher the S_{ext} , the higher the fraction of polymer confined in the mesopores.

To quantify the relative decrease of CNP pore surface and pore volume (D_S and D_V , respectively) upon PEO uptake, nitrogen adsorption–desorption isotherms of PEO-filled CNPs were compared to those of their CNP precursors. The relative decrease of S_{BET} , S_{ext} , and S_{mic} was calculated by recourse to eq 1, where $S(CNP)$ and $S(PEO/CNP)$ are the surface areas of pristine and PEO-filled samples, respectively. Similarly, the relative decrease of V_{mes} was obtained from volumetric parameters. With these considerations in mind, the % surface decrease reads

$$D_S(\%) = \frac{S(CNP) - S(PEO/CNP)}{S(CNP)} \times 100\% \quad (1)$$

Using this expression, the calculated relative decrease of S_{mic} ($D_{S_{mic}}$) shows that 100% of S_{mic} disappears upon PEO absorption in all samples. This finding suggests that the access of nitrogen to the micropores is blocked by the PEO chains as a result of a combination of micropore occupancy and micropore blockage by the polymer. The fraction of PEO within the micropores is likely to be higher for CNPs with a higher S_{mic} as explained above.

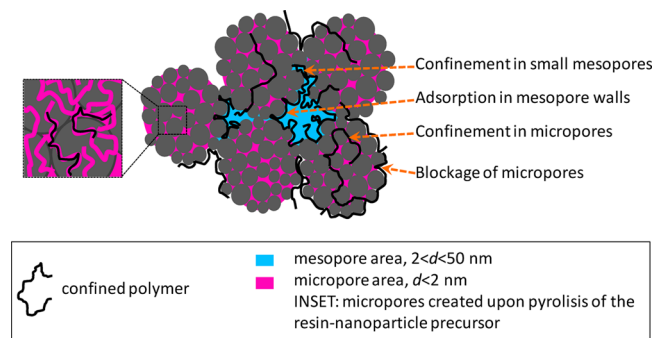
To examine in more detail the occupancy of mesopores by PEO, the relative decrease of S_{ext} ($D_{S_{ext}}$) and mesopore volume ($D_{V_{mes}}$) were also calculated. The data are shown in Figure 5a as a function of the ratio of the radius of gyration of PEO to average mesopore radius (R_g/r_{mes} ; $r_{mes} = \langle d_{BJH} \rangle / 2$). The value of R_g for PEO with $M_n = 94$ kg/mol was estimated to be 11 nm.²⁶ From these data, we observe that $D_{S_{ext}}$ and $D_{V_{mes}}$ display a linear dependence with R_g/r_{mes} except for samples A and B, whose pore-structure characteristics differ significantly from the rest of samples. These results indicate that a higher R_g/r_{mes} leads to a higher $D_{S_{ext}}$ and $D_{V_{mes}}$ upon PEO absorption as a consequence of mesopore blockage. In addition, $D_{S_{ext}}$ is higher than $D_{V_{mes}}$ for all samples, indicating that PEO confinement preferably occurs via macromolecular adsorption on the pore

walls. Given the chemical composition of CNPs (93 wt % carbon), we can also conclude that adsorption must preferentially occur via van der Waals interactions.

In terms of the relative decrease of S_{BET} ($D_{S_{BET}}$), Figure 5b shows an initial decrease of $D_{S_{BET}}$, an opposite trend to that observed for $D_{S_{ext}}$ and $D_{V_{mes}}$ in Figure 5a. Then, $D_{S_{BET}}$ reaches a plateau at $R_g/r_{mes} \geq 1.6$. Recalling that $S_{BET} \approx S_{mic} + S_{ext}$ and the fact that all CNP samples show a complete loss of microporosity upon polymer absorption, a net reduction of $D_{S_{BET}}$ appears to be related to the observed decrease in microporosity in going from sample I to E. Therefore, the loss of microporosity (S_{mic}) in these samples becomes more important than the loss of mesoporosity (S_{ext}), resulting in a sensible decrease in S_{BET} . Sample A exhibits a different behavior as a result of a different pore morphology, as explained earlier. Its $D_{S_{BET}}$ amounts to 98%, indicating that PEO chains obstruct both mesopores and micropores.

Scheme 2 illustrates the occupancy of CNP micropores and mesopores by the polymer phase. In this cartoon, the blue areas

Scheme 2. Cartoon Illustrating a Two-Dimensional Projection of PEO Confined in CNP Micropores and Mesopores under Dry Conditions



show the mesopores formed between nanoparticles and the pink areas show the micropores formed between smaller particles forming larger aggregates, as described above. In this situation, a number of different cases of polymer confinement can be observed, namely, polymer adsorption in the mesopore walls, confinement in the small mesopores (contact areas between carbon particles), and confinement within micropores as well as the unavoidable blockage of micropore entrances.

PEO uptake by pores with $d < 2R_g$ is entropically penalized.²⁷ In this situation, the chain has to unfold and slowly penetrate into the pores while effectively blocking access to the pores for other polymer molecules. The lower the pore diameter, the higher the entropy (S) loss as this quantity scales with pore size as $S \sim -N(a/d)^{5/3}$, where N is the degree of polymerization and a is the monomer size.²⁸ CNP micropore diameters ($d < 2$ nm) are well below $2R_g$ for PEO, and as a result, the polymer chains cannot completely unfold and penetrate the pores, causing the observed obstruction of nitrogen in adsorption–desorption data. The diameter of the CNP mesopores lies in the 2–50 nm range. In these pores, three scenarios are possible, namely, (a) $d \ll 2R_g$, (b) $d \approx 2R_g$, and (c) $d \gg 2R_g$. Case a is similar to micropore adsorption. In case b, the polymer chain is able to unfold and penetrate the pore. Its interaction with both sides of the pore walls guarantees its retention within the pore while largely blocking access to nitrogen. In case c, the polymer chains penetrate the pores and remain adsorbed on the pore walls generating their own porosity. Nitrogen molecules in adsorption–desorption experiments have access to the pores and signal the formation of a new surface contour characterized by a reduced pore volume.

Temperature-Modulated Differential Scanning Calorimetry. TM-DSC was used to identify thermal events arising from the confined PEO phase. A cooling ramp was used to obtain the reversing-heat-capacity (rev C_p) and nonreversing-heat-flow (non-rev HF) data. These data can be used to obtain the heat capacity of the sample from the reversing signal. Also, crystallization occurring during cooling can be evaluated from the nonreversing heat flow signal. Representative TM-DSC data of PEO/CNP samples are shown in Figure 6. To aid

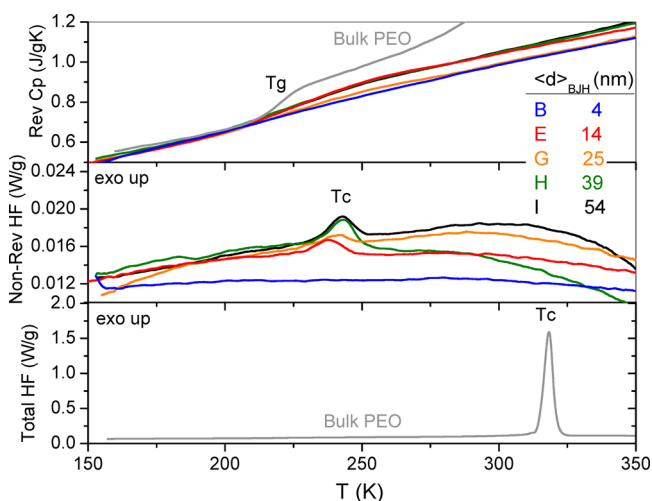


Figure 6. Reversing-heat-capacity (top) and nonreversing-heat-flow (middle) data for representative PEO/CNP samples. These data have been normalized to sample mass. The bottom figure shows the total heat flow for bulk PEO. All data have been obtained using a cooling rate of 3 K/min.

comparison, total-heat-flow (total HF) data for bulk PEO are also shown in the same figure. The step in heat capacity at the glass transition (ΔC_p), that is, the glass-transition temperature obtained when ΔC_p is one-half of the total ΔC_p ($T_g^{\Delta C_p/2}$), as well as the temperature width of the glass transition (ΔT_g), and a lower-bound temperature for the glass-transition range (T_g^L) were evaluated from the rev C_p signal as shown in Figure S3 of

the Supporting Information. These values are reported in Table 2.

The rev C_p data clearly show the occurrence of a glass transition in confined PEO samples over a similar temperature range as bulk semicrystalline PEO. In contrast to bulk PEO, the T_g^L values of PEO in PEO/CNP are slightly lower, although their $T_g^{\Delta C_p/2}$ values are slightly higher as a result of a broader thermal response (higher ΔT_g values). The broadening, shift, or even absence of the glass transition range has been often observed in PEO confined in small slits^{2,29} or adsorbed on a surface.^{30,31} The evaluation of the heat capacity change at the glass transition in samples A and B leads to large uncertainties due to a low PEO uptake by these samples. Therefore, these two cases will not be considered in our analysis below.

To estimate the percentage of PEO segments involved in the glass transition [hereafter $\Delta C_{p,T_g}$ (%)], we define

$$\Delta C_{p,T_g}(\%) = \frac{\Delta C_{p,\text{confined PEO}}}{\Delta C_{p,\text{bulk PEO}}} \times 100\% \quad (2)$$

ΔC_p at the glass transition for PEO confined in CNP ($\Delta C_{p,\text{confined PEO}}$) was obtained by normalizing the ΔC_p values of PEO/CNP ($\Delta C_{p,\text{sample}}$) by PEO mass (cf. Table 2). ΔC_p for completely amorphous bulk PEO ($\Delta C_{p,\text{bulk PEO}} = 0.86 \text{ J g}^{-1} \text{ K}^{-1}$) was obtained from the ATHAS databank. The results for $\Delta C_{p,T_g}$ (%) are shown in Figure 7a as a function of the percentage of CNP micropore surface to total surface. These data show that the amount of PEO leading to cooperative dynamics at T_g decreases (as much as 46% in sample I) as a function of the relative amount of CNP micropore surface area. Taking into account that polymer–substrate interactions are weak (van der Waals type), the above findings indicate that pore size is the controlling parameter for the reduction of $\Delta C_{p,T_g}$ (%). On this basis, a reduction of $\Delta C_{p,T_g}$ (%) for PEO in PEO/CNP implies that the polymer chains confined in the micropores do not contribute to the glass-transition step, a similar situation as that encountered for PEO confined in subnanometric GO layers.^{3,4} If we compare samples C and I (extreme cases of confinement), we observe notable differences relative to the above. Substrate C contains a large amount of ~ 7 nm diameter mesopores, whereas substrate I contains a much smaller fraction of larger mesopores (~ 54 nm). In terms of microporosity, substrate C contains half the number of micropores compared to sample I. Consequently, a high fraction of PEO retained in sample I is concentrated in the micropores. On the contrary, most of the PEO retained in sample C is located in the mesopores. Even when the mesopore diameter is as low as 7 nm, this pore diameter is large enough to provide a measurable contribution to the heat capacity by the retained PEO phase. However, the much smaller size of the micropores (< 2 nm) would dramatically modify the PEO conformation avoiding its contribution to the C_p jump at T_g .

The nonreversing-heat-flow data in Figure 6 show the presence of small crystallization peaks for PEO confined in CNP. The temperature at which this process occurs is well below the crystallization temperature (T_c) of bulk PEO (cf. Table 2). When comparing the T_c values of confined PEO samples, we observe that samples C–F display the lowest values. This behavior could be attributed to the lower mesopore diameters of their corresponding substrates, making the crystallization process upon cooling more difficult. For PEO confinement in CNPs A and B, the DSC data do not exhibit

Table 2. Calorimetric Parameters Obtained from the TM-DSC Data As Detailed in the Text

sample	T_g^L (K)	$T_g^{\Delta C_p/2}$ (K)	ΔT_g (K)	$\Delta C_{p,\text{sample}}$ (J/(g K))	$\Delta C_{p,\text{confined PEO}}^a$ (J/(g K))	T_c (K)
bulk PEO ^b	210 ± 1	217 ± 1	18 ± 1	0.12	—	318
A	202 ± 10	250 ± 10	75 ± 25	— ^c	— ^c	—
B	200 ± 10	250 ± 10	70 ± 20	— ^c	— ^c	—
C	198 ± 2	219 ± 2	53 ± 2	0.12	0.65	236
D	197 ± 2	226 ± 1	52 ± 2	0.10	0.58	237
E	197 ± 2	226 ± 1	54 ± 1	0.12	0.59	234
F	196 ± 2	221 ± 2	52 ± 2	0.12	0.57	235
G	195 ± 2	222 ± 2	53 ± 3	0.08	0.42	241
H	197 ± 2	223 ± 2	53 ± 2	0.10	0.52	243
I	195 ± 2	224 ± 1	53 ± 2	0.08	0.40	243

^aNormalized to PEO mass. ^bSemicrystallized. ^cLarge uncertainties.

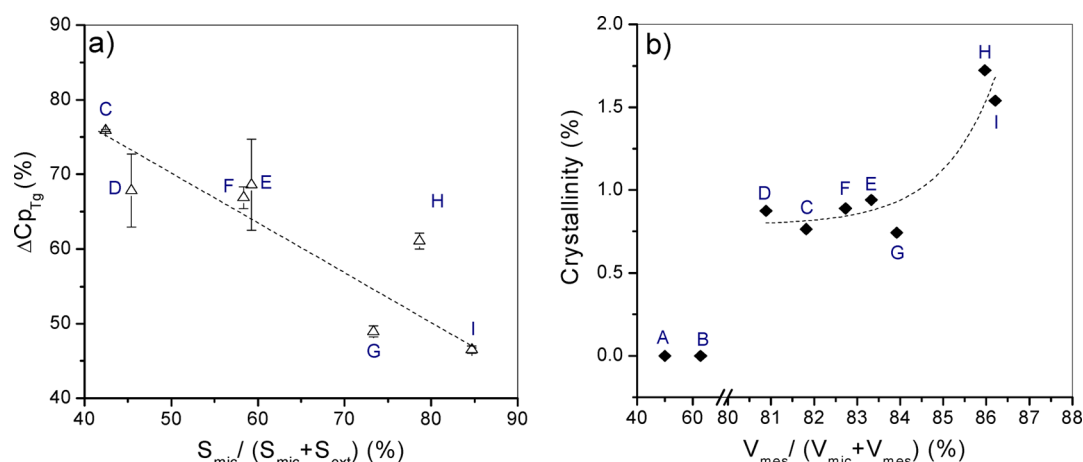


Figure 7. (a) Percentage of confined PEO segments contributing to the glass transition [$\Delta C_{p,T_g}$ (%)] in PEO/CNP as a function of the percentage of CNP micropore surface to total surface area. (b) Percentage of crystallinity of confined PEO in PEO/CNP as a function of the percentage of CNP mesopore volume to total volume. Dashed lines are rough guides to the eye.

any thermal processes in the nonreversing-heat-flow signal, indicating that the confined PEO chains cannot form crystals within the pores. As crystallization of PEO in PEO/CNP occurs within the glass transition range, the percentage of crystallinity of confined PEO can be obtained from eq 3 using the nonreversing data shown in Figure 6 according to the expression

$$\text{crystallinity (\%)} = \frac{\Delta H_{c,\text{confined PEO}}}{\Delta H_m^0} \times 100\% \quad (3)$$

$\Delta H_{c,\text{confined PEO}}$ was obtained from the integral of the crystallization peak in the nonreversing-heat-flow data of PEO in PEO/CNP normalized to the PEO content in the sample. ΔH_m^0 corresponds to the heat of melting of 100% crystalline PEO, obtained from the ATHAS databank (197 J/g). The data shown in Figure 7b show an increasing tendency for PEO to crystallize as the percentage of CNP mesopore volume to total CNP pore volume increases, up to a maximum value of at most 1.8%. These results indicate that crystallization of most of the PEO chains within the pores is suppressed and that only a small fraction of polymer chains (or subchains) can lead to crystalline domains. The significant reduction of the melting temperature (T_m) for confined PEO has been observed previously in other confinement media including nanochannels of sectional areas below 1 nm^{2,32} as well as in anodized aluminum oxide templates with pore diameter of 400 nm.³³ In the first case, strong PEO–substrate interactions at subnanometer confine-

ment scales were surmised to be the cause of a reduction in T_m . In the second case, a transition from a heterogeneous nucleation process in bulk PEO to a surface nucleation process in confined PEO was linked to an observed reduction in polymer crystallization temperature by about 50 °C. In our confined PEO system, both CNP pore heterogeneity and polymer–surface interactions prevent PEO chains from adopting a regular crystalline structure.

High-Resolution Inelastic Neutron Scattering. On the basis of previous studies using high-resolution INS to probe confined PEO intercalated in graphite oxide, the conformation of this polymer upon two-dimensional confinement changes from being a 7/2 helix in the bulk crystal to a planar zigzag.^{3,4} These changes are readily discernible in high-resolution INS data and lead to a distinct shift of the CH₂ rocking mode from 846 cm^{−1} (bulk) to 814 cm^{−1} (confined). The band at 846 cm^{−1} has been assigned to trans–gauche–trans (*tgt*) conformations of CCOC, OCCO, and COCC groups in crystalline PEO,³⁴ whereas that at 814 cm^{−1} corresponds to trans–trans–trans (*ttt*) conformations in PEO confined in the interlayer space of graphite oxide.^{3,4} The band at 948 cm^{−1} in bulk PEO is assigned to a combination of symmetric r(CH₂) and asymmetric COC stretch modes for *tgt* conformations. In confined PEO, this feature undergoes a red-shift and it is also suppressed considerably, evincing a significant reduction in the population of these conformers upon confinement.

In the case of PEO confined in CNP micro- and mesopores, a previous study where PEO was confined in a CNP specimen

with $\langle d \rangle_{\text{BJH}} = 8$ nm showed spectral similarities with that of PEO confined in the subnanometer interlayer space of graphite oxide.¹⁶ Following a similar methodology, high-resolution INS has also been used in this work to track possible changes to PEO macromolecular conformation when confined in CNP specimens with $\langle d \rangle_{\text{BJH}} = 54, 39$, and 14 nm (Figure 8). The

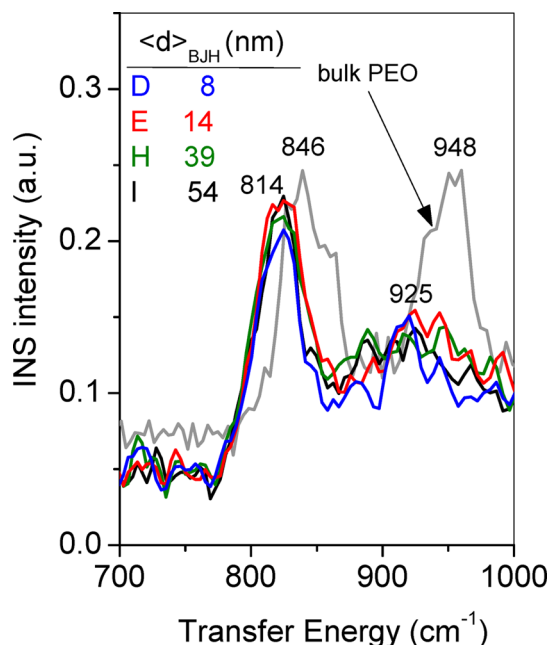


Figure 8. Mass-normalized INS spectra in the 700–1000 cm^{-1} region showing the CH_2 rocking mode at 846 and 814 cm^{-1} and COC stretch modes at 948 and 925 cm^{-1} . The spectra correspond to the INS response of PEO after subtraction of contributions from the substrate.

data are compared with that of bulk PEO and PEO confined in a CNP with $\langle d \rangle_{\text{BJH}} = 8$ nm. The INS data of PEO confined in these CNPs are quite similar across the series, yet they remain distinctly different to the INS response of the bulk polymer. These results highlight the formation of an amorphous polymer phase confined within the CNP pores where *ttt* conformations prevail across the different CNP morphologies investigated in this work. The small percentage of PEO crystallinity in these samples (<1.8%) is not detectable with this technique.

CONCLUSIONS

PEO was absorbed from water solution into the nanometer-size scale pores of CNPs with variable volume, pore surface, and diameter. The polymer phase occupies both CNP micropores ($d < 2$ nm) and mesopores ($2 < d < 50$ nm) and exhibits a mass-uptake saturation value of ~ 20 wt % for CNPs with S_{BET} of ~ 600 m^2/g . Confinement of PEO occurs via the filling of micropores and small mesopores as well as by adsorption on the mesopore walls. Nitrogen physisorption experiments reveal that microporosity in PEO-filled CNPs totally disappears upon PEO absorption, suggesting that access of nitrogen to the micropores can be blocked by the PEO chains as a result of a combination of micropore occupancy and the blockage of micropore entrances. In the case of mesopores, their occupancy by the PEO phase is not complete. Nitrogen molecules have access to the mesopores and signal the formation of a new surface contour characterized by a reduced pore volume. The higher the amount of mesopores in the substrate, the higher the

amount of PEO retained in the mesopores and the lower the reduction of ΔC_p at the glass transition. Conversely, the higher the amount of micropores in CNPs, the higher the amount of PEO confined in the micropores and the lower the contribution to ΔC_p at the glass transition. These results are interpreted as strong evidence that in this family of materials the glass transition is primarily driven by geometrical constraints imposed by the small micropore size ($d < 2$ nm) rather than by specific polymer–substrate interactions at the mesopore walls. Moreover, confinement of PEO in both CNP micropores and mesopores has a notable effect on the crystallization behavior of the PEO chains. In these confinement conditions, the PEO phase is mostly amorphous, showing maximal crystallization values of up to 1.8% in samples with the highest mesopore volumes. Vibrational data obtained by INS account for the emergence of planar zigzag conformations in the confined PEO, a result which is largely independent of CNP pore morphology.

ASSOCIATED CONTENT

Supporting Information

Figures S1–S3. This material is available free of charge via the Internet at <http://pubs.acs.org>.

AUTHOR INFORMATION

Corresponding Author

*E-mail fbarroso@ehu.es; Tel +34 94301 8803; Fax +34 94301 5800 (F.B.-B.).

Notes

The authors declare no competing financial interest.

ACKNOWLEDGMENTS

The authors gratefully acknowledge the support of the Spanish MEC (MAT2012-39199-C02-02 and MAT2012-31088), the Basque Government (IT-654-13), and the UK Science and Technology Facilities Council for the provision of beam time on the TOSCA spectrometer. P.P. acknowledges a PhD research contract from UCM (BE45/10). F.F.A. and S.R. acknowledge financial support from the UK Science and Technology Facilities Council.

REFERENCES

- (1) Alcoutlabi, M.; McKenna, G. B. *J. Phys.: Condens. Matter* **2005**, *17*, R461–R524.
- (2) Elmahdy, M. M.; Chrissopoulou, K.; Afratis, A.; Floudas, G.; Anastasiadis, S. H. *Macromolecules* **2006**, *39*, 5170–5173.
- (3) Barroso-Bujans, F.; Fernandez-Alonso, F.; Cerveny, S.; Arrese-Igor, S.; Alegría, A.; Colmenero, J. *Macromolecules* **2012**, *45*, 3137–3144.
- (4) Barroso-Bujans, F.; Fernandez-Alonso, F.; Cerveny, S.; Parker, S. F.; Alegría, A.; Colmenero, J. *Soft Matter* **2011**, *7*, 7173–7176.
- (5) Petychakis, L.; Floudas, G.; Fleischer, G. *Europhys. Lett.* **1997**, *40*, 685–690.
- (6) Napolitano, S.; Capponi, S.; Vanroy, B. *Eur. Phys. J. E* **2013**, *36*, 1–37.
- (7) Yabu, H.; Higuchi, T.; Jinnai, H. *Soft Matter* **2014**, *10*, 2919–2931.
- (8) Roth, C. B.; Dutcher, J. R. *Eur. Phys. J. E* **2003**, *12*, 103–107.
- (9) Bäumchen, O.; McGraw, J. D.; Forrest, J. A.; Dalnoki-Veress, K. *Phys. Rev. Lett.* **2012**, *109*, 055701.
- (10) Priestley, R. D.; Munda, M. K.; Barnett, N. J.; Broadbelt, L. J.; Torkelson, J. M. *Aust. J. Chem.* **2007**, *60*, 765–771.
- (11) Bose, S.; Kuila, T.; Mishra, A. K.; Rajasekar, R.; Kim, N. H.; Lee, J. H. *J. Mater. Chem.* **2012**, *22*, 767–784.

- (12) Barroso-Bujans, F.; Verdejo, R.; Arroyo, M.; Lopez-Gonzalez, M. D.; Riande, E.; Lopez-Manchado, M. A. *Macromol. Rapid Commun.* **2008**, *29*, 234–238.
- (13) Nardecchia, S.; Carriazo, D.; Ferrer, M. L.; Gutierrez, M. C.; del Monte, F. *Chem. Soc. Rev.* **2013**, *42*, 794–830.
- (14) Verdejo, R.; Barroso-Bujans, F.; Rodriguez-Perez, M. A.; de Saja, J. A.; Lopez-Manchado, M. A. *J. Mater. Chem.* **2008**, *18*, 2221–2226.
- (15) Verdejo, R.; Barroso-Bujans, F.; Rodriguez-Perez, M. A.; Antonio de Saja, J.; Arroyo, M.; Lopez-Manchado, M. A. *J. Mater. Chem.* **2008**, *18*, 3933–3939.
- (16) Barroso-Bujans, F.; Palomino, P.; Cervený, S.; Fernandez-Alonso, F.; Rudic, S.; Alegria, A.; Colmenero, J.; Enciso, E. *Soft Matter* **2013**, *9*, 10960–10965.
- (17) Pekala, R. W. *J. Mater. Sci.* **1989**, *24*, 3221–3227.
- (18) Rouquerol, F.; Rouquerol, J.; Sing, K. *Adsorption by Powders and Porous Solids*; Academic Press: San Diego, CA, 1999.
- (19) Brunauer, S.; Emmett, P. H.; Teller, E. *J. Am. Chem. Soc.* **1938**, *60*, 309–319.
- (20) Harkins, W. D.; Jura, G. *J. Chem. Phys.* **1943**, *11*, 431–432.
- (21) Barrett, E. P.; Joyner, L. G.; Halenda, P. P. *J. Am. Chem. Soc.* **1951**, *73*, 373–380.
- (22) Broekhoff, J. C. P.; de Boer, J. H. *J. Catal.* **1968**, *10*, 368–376.
- (23) Reading, M.; Hourston, D. J. *Modulated Temperature Differential Scanning Calorimetry: Theoretical and Practical Applications in Polymer Characterisation*; Springer: Berlin, 2006.
- (24) Colognesi, D.; Celli, M.; Cilloco, F.; Newport, R. J.; Parker, S. F.; Rossi-Albertini, V.; Sacchetti, F.; Tomkinson, J.; Zoppi, M. *Appl. Phys. A: Mater. Sci. Process.* **2002**, *74*, s64–s66.
- (25) Sing, K. S. W.; Everett, D. H.; Haul, R. A. W.; Moscou, L.; Pierotti, R. A.; Rouquerol, J.; Siemienińska, T. *Pure Appl. Chem.* **1985**, *57*, 603–619.
- (26) Fetters, L. J.; Lohse, D. J.; Richter, D.; Witten, T. A.; Zirkel, A. *Macromolecules* **1994**, *27*, 4639–4647.
- (27) Grüll, H.; Shaulich, R.; Yerushalmi-Rozen, R. *Macromolecules* **2001**, *34*, 8315–8320.
- (28) de Gennes, P. G. *Scaling Concepts in Polymer Physics*; Cornell University Press: Ithaca, NY, 1979.
- (29) Vaia, R. A.; Sauer, B. B.; Tse, O. K.; Giannelis, E. P. *J. Polym. Sci., Part B: Polym. Phys.* **1997**, *35*, 59–67.
- (30) Barroso-Bujans, F.; Fernandez-Alonso, F.; Pomposo, J. A.; Cervený, S.; Alegria, A.; Colmenero, J. *ACS Macro Lett.* **2012**, *1*, 550–554.
- (31) Madathingal, R. R.; Wunder, S. L. *Macromolecules* **2011**, *44*, 2873–2882.
- (32) Uemura, T.; Yanai, N.; Watanabe, S.; Tanaka, H.; Numaguchi, R.; Miyahara, M. T.; Ohta, Y.; Nagaoka, M.; Kitagawa, S. *Nat. Commun.* **2010**, *1*, 83.
- (33) Maiz, J.; Martin, J.; Mijangos, C. *Langmuir* **2012**, *28*, 12296–12303.
- (34) Maxfield, J.; Shepherd, I. W. *Polymer* **1975**, *16*, 505–509.